Materials Futures

PAPER • **OPEN ACCESS**

3D printed modular Bouligand dissipative structures with adjustable mechanical properties for gradient energy absorbing

To cite this article: Junfeng Xiao *et al* 2024 *Mater. Futures* **3** 025001

OPEN ACCESS
IOP Publishing | Songshan Lake Materials Laboratory
Materials Futures
Mater. Futures 3 (2024) 025001 (13pp)
https://doi.org/10.1088/2752-5724/ad22cf

3D printed modular Bouligand dissipative structures with adjustable mechanical properties for gradient energy absorbing

Junfeng Xiao[1,7], Mengxing Zhang[2,3,7], Fei Zhai[2,*], Hongrui Wei[2,4], Sen Liu[2], Peng Wang[4], Zhiyang Liu[5], Zhongying Ji[2,6,*] and Xiaolong Wang[2,6]

[1] Shenzhen Institute of Information Technology, Shenzhen 518172, People's Republic of China
[2] Shandong Laboratory of Advanced Materials and Green Manufacturing at Yantai, Yantai Zhongke Research Institute of Advanced Materials and Green Chemical Engineering, Yantai 264006, People's Republic of China
[3] School of Chemistry and Chemical Engineering, Key Laboratory of Materials-Oriented Chemical Engineering of Xinjiang Uygur Autonomous Region, Shihezi University, Shihezi 832003, People's Republic of China
[4] School of Transportation Engineering, Shandong Jianzhu University, Jinan 250101, People's Republic of China
[5] College of Civil and Transportation Engineering, Shenzhen University, Shenzhen 518061, People's Republic of China
[6] State Key Laboratory of Solid Lubrication, Lanzhou Institute of Chemical Physics, Chinese Academy of Sciences, Gansu Lanzhou 730000, People's Republic of China

E-mail: zhaifei@amgm.ac.cn and jizy@licp.cas.cn

Received 19 December 2023, revised 17 January 2024
Accepted for publication 21 January 2024
Published 8 February 2024

Abstract

Three-dimensional (3D) printing allows for the creation of complex, layered structures with precise micro and macro architectures that are not achievable through traditional methods. By designing 3D structures with geometric precision, it is possible to achieve selective regulation of mechanical properties, enabling efficient dissipation of mechanical energy. In this study, a series of modular samples inspired by the Bouligand structure were designed and produced using a direct ink writing system, along with a classical printable polydimethylsiloxane ink. By altering the angles of filaments in adjacent layers (from 30° to 90°) and the filament spacing during printing (from 0.8 mm to 2.4 mm), the mechanical properties of these modular samples can be adjusted. Compression mechanical testing revealed that the 3D printed modular Bouligand structures exhibit stress-strain responses that enable multiple adjustments of the elastic modulus from 0.06 MPa to over 0.8 MPa. The mechanical properties were adjusted more than 10 times in printed samples prepared using uniform materials. The gradient control mechanism of

[7] These authors contributed equally.
[*] Authors to whom any correspondence should be addressed.

mechanical properties during this process was analyzed using finite element analysis. Finally, 3D printed customized modular Bouligand structures can be assembled to create an array with Bouligand structures displaying various orientations and interlayer details tailored to specific requirements. By decomposing the original Bouligand structure and then assembling the modular samples into a specialized array, this research aims to provide parameters for achieving gradient energy absorption structures through modular 3D printing.

Supplementary material for this article is available online

Keywords: 3D printing, additive manufacturing, Bouligand structure, energy absorbing structures

1. Introduction

Silicone rubber (Polydimethylsiloxane, PDMS) is a type of polyorganosiloxane with a highly cross-linked network structure [1–3]. Due to the interaction of silicon-oxygen bonds (–Si–O–Si–), silicone rubber exhibits a series of excellent properties, such as biocompatibility, optical transparency, relative chemical inertness, electrical insulation, non-flammability, non-absorption of ultraviolet rays, low surface tension, hydrophobicity, and high oxygen permeability [4]. Therefore, silicone rubber, with a comprehensive range of properties, has broad application value in fields such as biomedical products, functional coatings, electronic and optical devices, aerospace, and shock absorption and buffering [5–8]. However, the processing technology of silicone rubber products still relies mainly on traditional casting methods, which have drawbacks such as complex molding processes, lengthy production times, and uncontrollable mechanical properties. These limitations seriously hinder the development of silicone rubber-based materials for manufacturing complex, multi-scale, ordered porous structures, and other high-precision components [9].

In order to meet the requirements for precise printing of complex structures, additive manufacturing (AM) technology has been utilized in the processing of silicone rubber materials [10]. Rapid prototyping, the formation of large structures, reduction of printing defects, and improvement of mechanical properties are key factors that promote the development of AM technology [11–13]. Based on the data from digital three-dimensional (3D) models, 3D printed objects are created layer by layer using a computer-controlled translation stage [14]. Unlike traditional methods that require molds or lithography masks, 3D printing can rapidly convert computer-aided designs into intricate 3D prototypes without wasting excess materials [15]. The combination of silicone rubber and 3D printing offers a promising manufacturing technology that can achieve rapid processing, thereby saving time and cost [16–18]. Currently, 3D printing of silicone rubber is extensively utilized in the medical field. High-precision 3D printing and the excellent chemical stability of silicone rubber are used to prepare microfluidic devices, implants, blood vessels, and other biological devices [19, 20]. Furthermore, 3D printing technology plays a crucial role in fabricating soft active materials, addressing the challenges associated with molding silicone rubber. These materials are used in actuators, soft robots, wearable electronic devices, and sensing devices. Compared to traditional manufacturing techniques, the increased design flexibility enables the 3D printing of mechanical metamaterials, such as honeycomb structures, structures with negative Poisson's ratio, Bouligand structures, etc. This has great potential in shock absorption and cushioning applications [21, 22].

Due to the challenges in molding technology, such as poor rheology behavior, low photo-curing rate, and differences in the molding mechanism of printing technologies, recent years have seen a focus on direct ink writing (DIW) printing and light-curing printing for 3D printing molding technology of PDMS. This focus has resulted in a series of advancements [23–26]. However, there are still some issues to address. For UV-curing printing, current research primarily focuses on synthesizing monomers and preparing photosensitive silicone rubber ink [27–30]. Furthermore, special UV-curing printers must be installed to print high-viscosity silicone rubber, which limits their versatility. In most DIW technologies, the ink materials generally meet the printing requirements by incorporating fillers. However, this approach is influenced by complex factors and does not facilitate the regulation of mechanical properties through structures [31–34].

In this study, we utilized the commercial monomer SE1700 and a polymerization inhibitor to prepare the printing ink for the realization of fine PDMS structures. The DIW 3D printing technology was employed to print PDMS. The printing process was optimized by adjusting extrusion parameters to produce printed samples with consistent morphologies, and then creating various intricate and high-resolution energy dissipation devices. Based on this, the printed samples were further designed to investigate the relationship between sample structure and mechanical properties. The Bouligand structure was decomposed to obtain modular layered structures. The designed modular models were then accurately converted into printed samples using optimized printing parameters. The stress-strain responses of the printed modular Bouligand structures were explored through compression mechanics testing. The gradient control mechanism of their mechanical properties was analyzed using finite element analysis (FEA), ultimately achieving flexible assembly of gradient combination energy-absorbing structure arrays.

2. Materials and methods

2.1. Materials

PDMS adhesive (SE 1700) with a curing agent was purchased from Dow Corning, USA. Diallyl maleate (DAM) was purchased from Shanghai Aladdin Biochemical Technology Co., Ltd

2.2. Preparation of printing ink

First, the two components of SE1700 and the curing agent were thoroughly mixed. Then, 10 g of the mixture was weighed, and 0.1 g of DAM was added as an inhibitor. The ink was further mixed evenly using ball milling. Move the ink to a 10 cc printing syringe and centrifuge it at 7000 rpm for 10 min to remove bubbles from the ink.

2.3. 3D printing of PDMS structures

The printing model is created using CAD, and the STL format of the model is imported into the printer's software to adjust the printing parameters and generate the printing path. By adjusting the printing parameters, such as the inner diameter of the printing micro nozzle, the diameter of the extruded filament, and the printing speed. The ink is extruded in a filiform manner onto the silane-treated glass sheet through the nozzle under a specific pressure. After the printing is completed, the printed sample is placed in a high-temperature oven and cured at 150 °C for 2 h to form a silicone rubber sample with an adjustable structure.

3. Characterization

The ink's rheological properties were measured using a rotational rheometer. The ink's viscoelasticity and thixotropy were measured using a cone-plate sensor system. Viscoelastic tests, such as shear thinning and shear modulus, were conducted using rotation mode and oscillation mode. The test temperature for shear thinning was 25 °C, and the shear rate range was 0.1–100 s^{-1}. The apparent viscosity was measured as a function of shear rate. The temperature for the oscillation shear test was 25 °C, with a shear frequency of 1.0 Hz, and a shear stress scanning range of 0.1–1000 Pa. The thixotropy recovery test for ink also involves viscosity and modulus tests. When measuring viscosity, the shear rate alternates periodically between high shear rate (1000 s^{-1}) and low shear rate (0.1 s^{-1}).

The morphology of the printed sample was observed using an optical microscope (BX51, Olympus) with a 4*X* eyepiece magnification. Differential scanning calorimetry (DSC200F3, NETZSCH) and simultaneous thermal analysis (STA449F3, NETZSCH) were employed to investigate the impact of inhibitors on the thermal stability of inks. The DSC test involved observing the change in glass transition temperature (T_g) from −140 °C to 40 °C at a heating rate of 10 °C min^{-1} in a nitrogen atmosphere. The thermal curing behavior of the ink at high temperatures was investigated by scanning up to 200 °C at a heating rate of 10 °C min^{-1} from room temperature. The ink composition and thermal stability were analyzed using thermal gravity analysis (TGA). The TGA testing process was conducted at a consistent rate in a nitrogen atmosphere, at a temperature range of 25 °C–800 °C.

Compression performance tests include compressive stress-strain tests, cyclic compression tests, and stress relaxation tests. The tests were conducted using a universal testing machine (DY-35, Adamel Lhomargy). The compression stress-strain test rate was set to 10 mm min^{-1}, while the stress relaxation test rate was 1.0 mm min^{-1}. To mitigate the impact of stress relaxation on the stress-strain curve, the sample was pre-compressed three times before testing, and the fourth stress-strain curve was used to analyze the uniaxial compression performance. The stress relaxation test points were chosen based on the stress-strain curve, and the sample was compressed to the selected strain point at a compression rate of 1.0 mm min^{-1} and held for 3.0 h. The stress relaxation rate of the printed silicone rubber sample was calculated using the following formula:

$$\delta = \frac{(\tau_0 - \tau_1)}{\tau_0}$$

where δ is the stress relaxation rate (%), τ_0 is the maximum stress (MPa), τ_1 is the stress after 3 h, the unit is MPa.

The FEA was used to study the simulation and load distribution of the compression process of the PDMS modular Bouligand dissipative structures.

4. Results and discussion

4.1. 3D printing of PDMS fine structures

To achieve high-precision 3D printing of PDMS materials and structures, we have developed an ink formula, as depicted in figure 1(a), primarily utilizing the commercial monomer resin SE1700 and its initiator. We also incorporate the DAM inhibitor to prevent premature solidification during the printing process, thereby facilitating the printing process. In this ink system, the DAM inhibitor primarily functions by forming a relatively stable complex with the platinum catalyst to slow down or inhibit the hydrosilylation addition reaction. The different components of the ink system are thoroughly mixed using a ball mill, and the bubbles produced during ball milling are eliminated through centrifugation to obtain a consistent printing ink for use. In this study, DIW printing was accomplished by extruding the printing ink mentioned above under air pressure to produce uniform printing filaments and regular printing structures. Printed samples were later heat-cured and shaped, as shown in figure 1(b). The primary factor influencing the extrusion effect in DIW printing is the viscoelasticity of the ink. The viscoelasticity of the ink needs to be regulated due to its solid elasticity and fluid viscosity characteristics. Among these properties, shear thinning behavior and shear modulus are the most crucial rheological properties for designing DIW 3D printing precursor inks. Additionally, these two properties are commonly utilized to characterize the viscoelasticity of inks. Shear thinning refers to the phenomenon

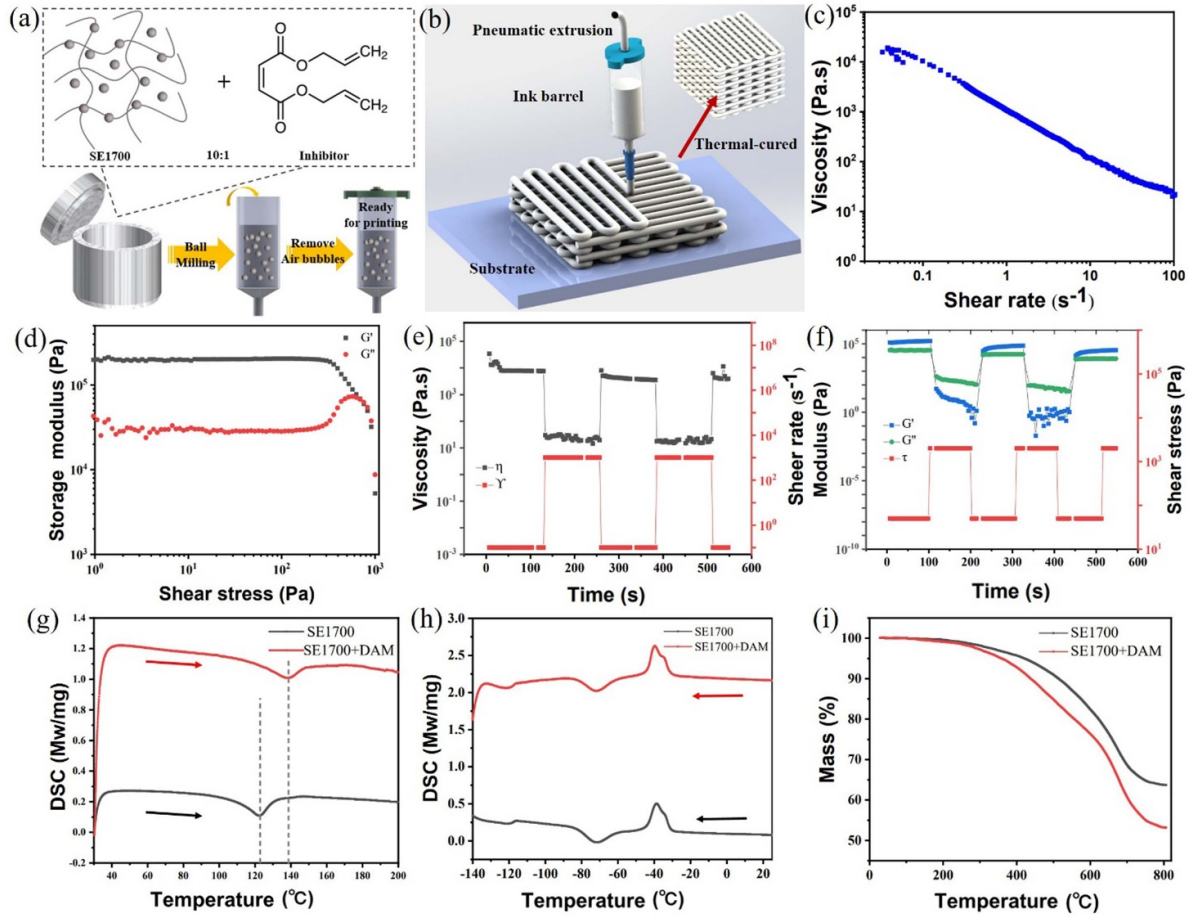

Figure 1. (a) Schematic illustration of the preparation process of DIW 3D printing ink. (b) Schematic diagram of DIW 3D printing process. (c) Shear thinning curve of the printing ink. (d) The shear modulus curve of the printing ink. (e) The viscosity thixotropic recovery performance of ink at low shear rate (0.1 s^{-1}) and high shear rate (1000 s^{-1}). (f) The modulus thixotropic recovery performance of ink under low shear stress (50 Pa) and high shear stress (2000 Pa). (g) DSC curve (heating process) of printing ink. (h) DSC curve (cooling process) of printing ink. (i) Thermogravimetric curve of printing ink.

where the viscosity of ink decreases as the shear rate increases, facilitating the extrusion of ink during the printing process. As shown in figure 1(c), it is evident that the viscosity of the ink decreases with the increase in shear rate, indicating that the prepared ink demonstrates significant shear thinning behavior, further confirming its printability. The ink itself has a specific yield stress, and when the shear stress exceeds this yield stress, it will exhibit characteristics similar to those of liquids. These yield stress fluids can be effectively described using the Herschel–Bulkley model [35]:

$$\tau = \tau_y + K\gamma^n$$

In the equation, τ represents the shear stress, τ_y stands for the yield stress, K denotes the consistency, γ represents the shear rate, and n represents the flow index (for shear thinning fluids, $n < 1$). To ensure that the printable ink can pass through the micro nozzle smoothly, the stress applied inside the micro nozzle must exceed the yield stress of the ink (τ_y). When the ink flows out of the micro nozzle, τ_y and shear modulus, also known as the energy storage modulus (G'), quickly recover to their original values. Adequate yield stress is essential for restoring the solid state of ink after deposition, which is beneficial for supporting the upper and lower layers. Therefore, G' must be sufficiently high (greater than 10^3 Pa) to ensure the final printed rigid structure. To meet printing requirements, the G' of the ink should not be too high, as it can lead to ink blockage in the micro nozzle during the squeezing process. Therefore, it is common to use the energy storage modulus (G') and loss modulus (G'') to jointly characterize the shear modulus characteristics of ink, which represent material elasticity and viscosity indicators. The behavior indicates the ability to maintain its extruded shape. In figure 1(d), the oscillating stress scanning test of the ink at room temperature shows that the material exhibits solid-like behavior at lower oscillating stresses ($G' > G''$), while the oscillating stress above the yield stress exhibits fluid-like behavior ($G' < G''$).

The precursor ink for DIW 3D printing must have self-supporting properties to ensure a fine molding effect. Thixotropy is generally used to characterize this property. Thixotropy refers to the process in which the ink changes from a viscous state to a more fluid state under shear stress, and when the shear stress is removed, the ink automatically returns to its original state, a phenomenon known as

thixotropic recovery. Figures 1(e) and (f) depict the viscosity thixotropy recovery performance and modulus recovery performance of the ink, respectively. As the ink continuously alternates between high and low shear rates, its viscosity also undergoes periodic changes. At low shear rates, the ink exhibits relatively high viscosity. When the shear rate is increased, the viscosity of the ink decreases, demonstrating the shear thinning phenomenon of printing ink at high shear rates. Additionally, there is no significant delay in the viscosity thixotropic recovery. In addition, similar to the thixotropic recovery performance of viscosity, the ink's modulus recovery also shows periodic changes with the increase or decrease of shear stress. The storage modulus is higher than the loss modulus at low shear stress. When subjected to high shear stress, the storage modulus rapidly decreases in comparison to the loss modulus, without significant hysteresis. These results all indicate that the ink exhibits favorable self-supporting performance and will not collapse or deform when extruded onto the platform.

After completing the extrusion and molding process, thermal curing post-treatment is necessary to further solidify the structure of the printed sample. To determine the thermal curing conditions, the DSC curve of the printed sample is analyzed. As shown in figure 1(g), it can be observed that without the inhibitor, the curing heat release of the ink started at 80 °C and reached its maximum reaction rate around 124 °C. After the addition of the DAM inhibitor, the exothermic peak of the ink shifts to the right and reaches the maximum reaction rate at around 139 °C. This indicates that DAM can inhibit the thermal curing reaction of silicone rubber. Figure 1(h) shows that the glass transition temperature (T_g) of the ink (−123 °C) remains relatively unchanged after the addition of inhibitors. This suggests that the inhibitors have minimal impact on the ink's physical properties and are unlikely to diminish the printing quality. From the thermogravimetric curve in figure 1(i), it can be observed that the mass loss of the ink does not change significantly after adding the inhibitor and heating it to 200 °C. However, the mass loss of the ink with the inhibitor is higher when the temperature is further increased. This further indicates that DAM can inhibit the thermal curing rate of the ink. Thus, the thermal curing conditions can be determined, and a temperature of 150 °C is selected as the initial thermal curing temperature for the printed samples to ensure rapid curing.

There are numerous factors that influence the printing quality of DIW printing, such as extrusion pressure, printing speed, nozzle inner diameter, filament spacing, and layer thickness. The spacing of filaments and layer thickness can be controlled by printing software. However, the inner diameter of the printing nozzle must be determined taking into account various other parameters, such as the rheological properties of the printing ink, extrusion pressure, and printing speed. The extrusion pressure and printing speed are mutually constrained, the extrusion amount increases with higher extrusion pressure. At this time, if the printing speed is slow, the extruded filaments will accumulate and overlap. On the other hand, if the printing speed is too fast, the extruded filaments may not be deposited on the substrate, thereby affecting the molding effect of the printed structure. In order to facilitate the comparison of printing effects, the extrusion pressure of the ink is kept constant (unless otherwise specified, the extrusion pressure in the following experiment is fixed at 0.15 MPa), and the impact of the inner diameter of the printing nozzle and printing speed on the forming effect of DIW 3D printing is studied.

Firstly, the study examined the influence of the inner diameter of the printing nozzles on the forming effect. The printing nozzles with inner diameters of 210 μm, 410 μm, and 610 μm were chosen for printing and comparing the forming effects. Figure 2(a) displays the optical microscopy (OM) images of the individual filaments printed using micro nozzles with varying inner diameters. The diameter of the printed filament is similar to the inner diameter of the printing nozzle. And there is no significant shrinkage of the single filament after the thermal curing process (see figure S1), indicating that the thermal curing post-treatment has no significant effect on the molding outcome. From the OM images of the grid structures printed by different printing nozzles at the same filament spacing, it can be seen that the printing nozzle with an inner diameter of 210 μm produces distinct patterns. Significant collapse and deformation are observed between the filaments. This is because the spacing between the filaments is too large, and the diameter of the filaments is too thin. This is not enough to provide adequate support under its own gravity to stabilize the printing shape. Therefore, the thin nozzle is more suitable for printing models with smaller filament spacing, as shown in figure S2(a). By comparison, the printing nozzle with an inner diameter of 410 μm forms a regular mesh structure during printing, and the nodes are neatly connected without deformation. The printing nozzle with an inner diameter of 610 μm produces thicker filaments, resulting in dense spacing. This is not conducive to the precise design of patterned structures and is more suitable for printing models with larger filament spacing, as shown in figure S2(b). Based on the model size and filament spacing in this study, a printing nozzle with an inner diameter of 410 μm was chosen for structural design and mechanical performance regulation.

The diameters of individual filaments obtained at various printing speeds are depicted in figure 2(b). When the extrusion pressure is set at 0.15 MPa and the inner diameter of the printing nozzle is fixed at 410 μm, the diameter of the extruded filament gradually decreases as the printing speed increases, from 550 μm at 3.0 mm s^{-1} to approximately 300 μm at 7.0 mm s^{-1}. This is mainly because when the printing speed is slow, there is more ink accumulation in a local position, while when the printing speed is fast, the ink is excessively stretched, resulting in a thinner filament. Figure 2(c) displays the OM images of the printed samples. It is evident that the diameter of a single filament decreases as the printing speed increases. The diameter of a single filament obtained at a printing speed of 5.0 mm s^{-1} is closer to the inner diameter of the printing nozzle. When the printing speed is less than 5.0 mm s^{-1}, there will be overlap between adjacent layers of filaments, resulting in a flattened and elliptical diameter of a single filament. When

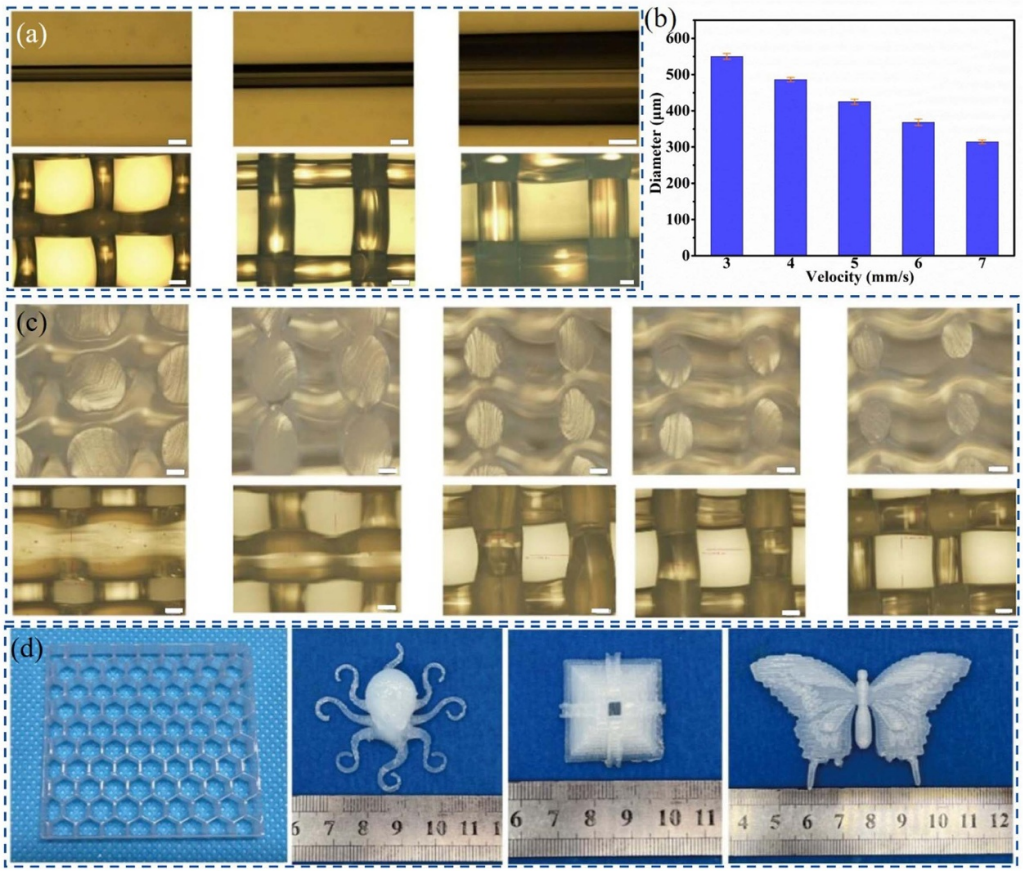

Figure 2. (a) Optical microscopic images of printed samples using printing nozzles with inner diameters of 210 μm, 410 μm, and 610 μm. (b) Diameters of printed samples obtained using 410 μm nozzle at different printing speeds. (c) Optical microscopic images of printed PDMS samples obtained using 410 μm nozzle at different printing speeds. (d) Printed samples with complex structures. Scale bar 200 μm.

the printing speed exceeds 5.0 mm s^{-1}, the interlayer bonding between filaments undergoes severe deformation, and the diameter of a single filament differs greatly from the inner diameter of the printing nozzle, ultimately leading to distortion of the printed PDMS samples. In summary, the optimal printing speed in this study is 5.0 mm s^{-1}.

Based on the above research, the selected printing parameters for PDMS samples are as follows: the extrusion pressure is 0.15 MPa, the inner diameter of the printing nozzle is 410 μm, the printing speed is 5.0 mm s^{-1}, and the printed layer thickness is 0.35 mm. The dimensions of the printed modular structure are 15 mm $\times$ 15 mm $\times$ 15 mm. To further validate the printing effect of these printing parameters, several more complex structures are printed using the same printing ink. Figure 2(d) displays the physical images of the complex PDMS structures printed using DIW. It is evident that by using these parameters, we can create grid structures, honeycomb structures, and more complex designs, including artificial ears (see figure S3), octopus, pyramid, and butterfly models. All of these printed samples exhibit consistent high resolution and strong precision structure, with no apparent deformation or collapse. This confirms the feasibility and stability of the PDMS ink system and printing parameters, which are prerequisites for subsequent printing of modular samples and ensure the integrity of the printed modular sample structure.

4.2. Modular Bouligand dissipative structures

A buffering energy-absorbing structure is a type of construction designed to absorb energy during collisions or impacts. It is typically made up of multi-layer materials, some of which are able to deform or rupture, absorbing energy and protecting other parts from damage. The design of energy-absorbing buffering structures requires consideration of various factors, including materials, shape, thickness, and methods of connection between layers. In general, each layer of a buffering energy-absorbing structure should possess varying deformation capacity and rupture strength. This allows for the absorption of energy layer by layer during collisions or impacts. In addition, the energy-absorbing structure must also consider factors such as weight and cost to ensure its practical feasibility and cost-effectiveness in real-world applications. The Bouligand structure is a typical spiral-layered fiber-reinforced structure that exists in many biological structures and exhibits excellent mechanical properties. Here, a series of modular energy absorption structures are designed based on the characteristics of the Bouligand structure to achieve a gradient compression energy absorption effect. The modular design of the printed samples can reduce printing complexity while allowing for flexible assembly based on specific needs. As shown in figure 3(a), with a rotation unit of 15°, the rotation angle

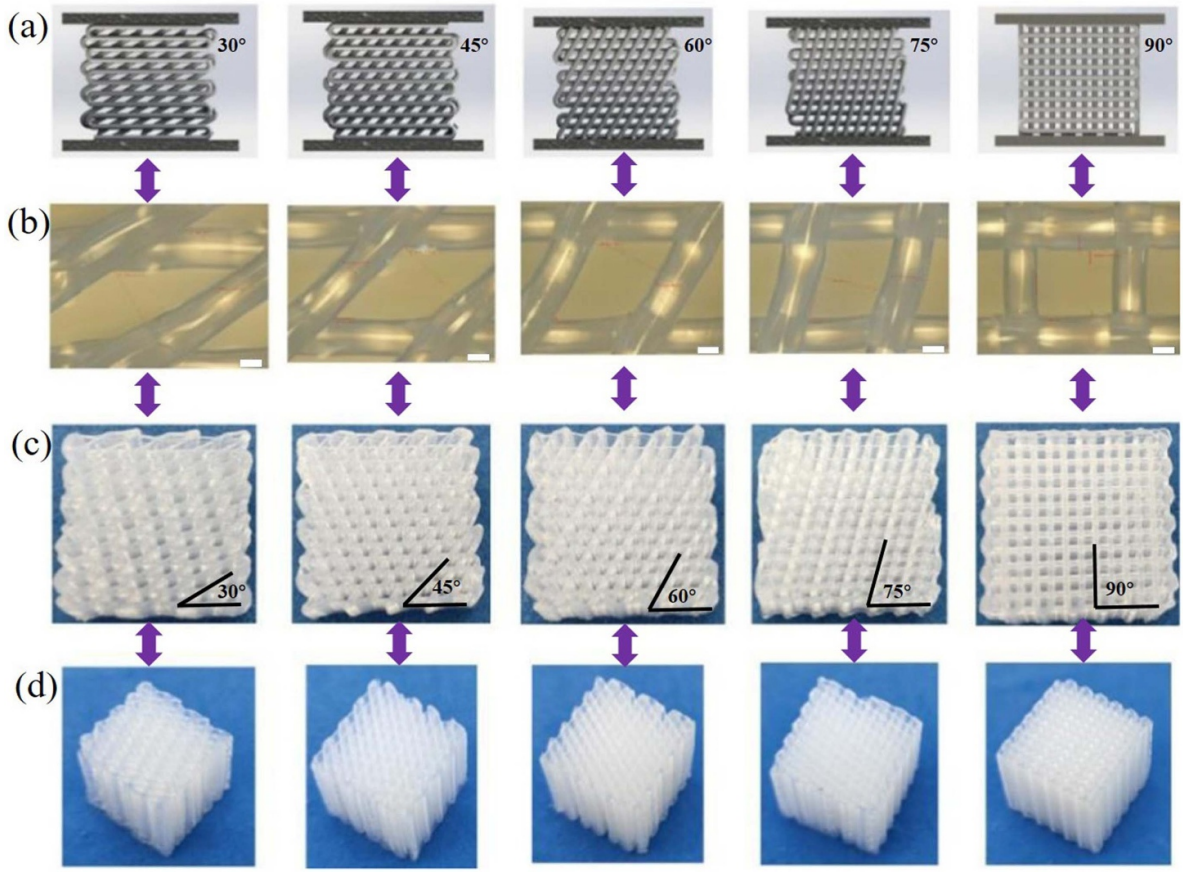

Figure 3. Modular Bouligand dissipative structures with different filament rotation angles. (a) Schematic illurstration of modular samples with different filament rotation angles: 30°, 45°, 60°, 75°, 90°. (b) Optical microscope images of printed PDMS modular samples with different filament rotation angles after thermal curing (scale bar 200 μm). (c) Top view and (d) side view of the printed samples (15 mm × 15 mm × 15 mm) with different filament rotation angles.

of the second layer relative to the first layer is adjusted. Five relative angles of 0–30°, 0–45°, 0–60°, 0–75°, and 0–90° are chosen to produce printed samples with various filling structures. It should be noted that the structural sample with a 0–15° angle was not selected for compression testing due to its poor molding effect (see figure S4). The spacing between printed filaments and the printing angle can be directly adjusted using the slicing software. The compression test samples are 15 mm × 15 mm × 15 mm cubes. The optical microscope images in figure 3(b) demonstrate that the printed modular samples exhibit high fidelity. The photos of the printed samples are shown in figures 3(c) and (d). It is evident that the structural pores of the printed samples are relatively uniform, providing good support without any noticeable defects or collapses. This further demonstrates the stability and feasibility of DIW 3D printed PDMS.

4.3. Compression test of modular Bouligand dissipative structures

The differences in elastic modulus and stress relaxation of PDMS modular Bouligand structures were characterized through compression tests to verify the gradient energy-absorbing performance of these modular samples. The elastic modulus refers to a material's capacity to withstand elastic deformation under load, as determined by the initial slope of the stress-strain curve. Stress relaxation refers to the phenomenon of applying a constant compressive stress to a material at a certain strain under specific environmental conditions, and observing that the stress gradually decreases with time. The concept of stress relaxation involves the structure undergoing plastic deformation when subjected to force, leading to a reduction in internal stress. The primary reason for stress attenuation is the gradual consumption of the material's stress by the viscous internal resistance that must be overcome when the molecular chain moves. The characteristic of this phenomenon is that it begins rapidly and then decelerates. It is more beneficial to promote the practical application of a material with a lower stress relaxation rate. Figure 4 displays the compression test results of modular silicone rubber energy-absorbing structure samples at 0%, 20%, 40%, and 60% strain, respectively. It is evident that the compression processes of the modular series samples vary, and the morphologies of the samples under the same strain are noticeably different.

FEA was used to investigate the impact of topology on the stress relaxation behavior of these 3D printed modular structures under compression. The FEA results were obtained by fitting the mechanical data of the modular structures with the

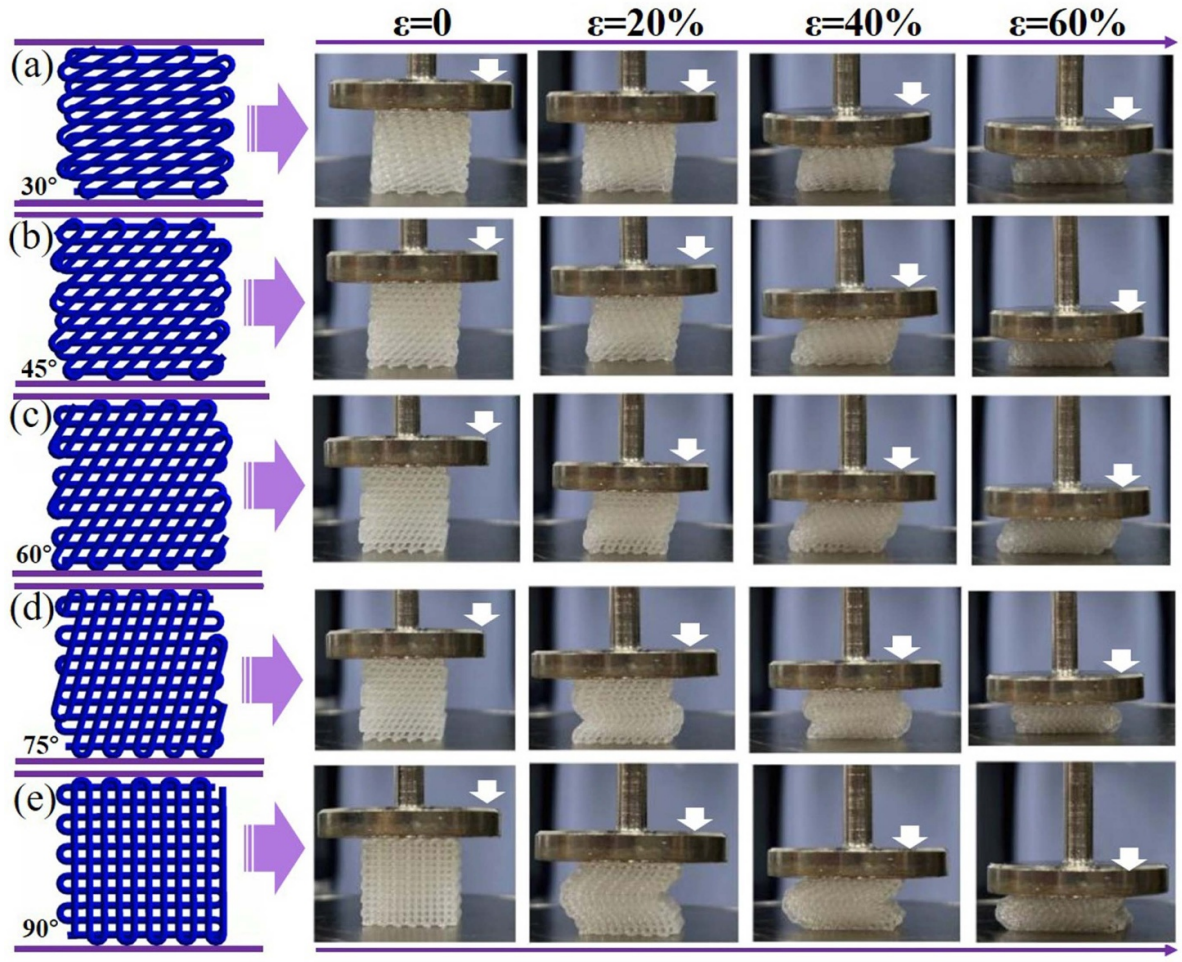

Figure 4. Compression test of PDMS modular Bouligand dissipative structures printed at different rotation angles under strain (ε) of 0%, 20%, 40%, and 60%.

Mooney–Rivlin constitutive equation, using a triangular mesh and a solid mechanics solver. By combining the experimental observations (figure 4) with the FEA results (figure 5), we can analyze the compression deformation mechanism of the modular structures. Models of the modular samples were constructed using eight layers of filaments with a diameter of 0.41 mm, a spacing of 1.2 mm, and a layer height of 0.35 mm. Free boundary conditions were imposed on the simulated PDMS modular structures. Two thin and rigid plates were attached to the upper and lower sides of the foam, and both plates were secured in place. The material parameters were determined by fitting the mechanical data of the PDMS modular structures with the Mooney–Rivlin constitutive equation. It can be observed that the theoretical simulation results are largely consistent with the experimental findings. The transfer of load with the deviation direction of the line demonstrates the effectiveness of the structural design. The deviation between the experimental and simulation results of the 0–75° sample is attributed to the formation defects in specific parts of the printed sample. The symmetrical structure of the 0–90° sample makes it unpredictable whether the modular sample will tilt to either side during the compression process. This outcome is influenced more by factors such as molding defects during the experiment. In general, when the modular sample is compressed, the load is transmitted along the printed filaments in the sample, resulting in an angled adjacent layer line that tends to be parallel, forming a stress layer. The simulation results indicate that in this process, the inclined line will shift the load to the inclined side and achieve a gradient buffering effect.

4.4. Regulation of mechanical properties

As mentioned previously, the regulation of mechanical properties through gradient can be achieved by designing the structure of modular PDMS samples based on the Bouligand structure, as illustrated in figure 6(a). These modular samples with a fine filament spacing of 1.2 mm were printed at 15° intervals. The samples include 0–15° and 0–165°, 0–30° and 0–150°, 0–45° and 0–135°, 0–60° and 0–120°, and 0–75° and 0–105°, all of which have the same structure, but the print direction is opposite. The analysis of their stress situation during the compression test is shown in figure 6. The compressive stress-strain curve of materials is typically divided into three stages, as shown in figure 6(b): the first stage is the linear elastic stage, during which the stress exhibits a linear change; the second stage is characterized by collapse due to the elastic buckling

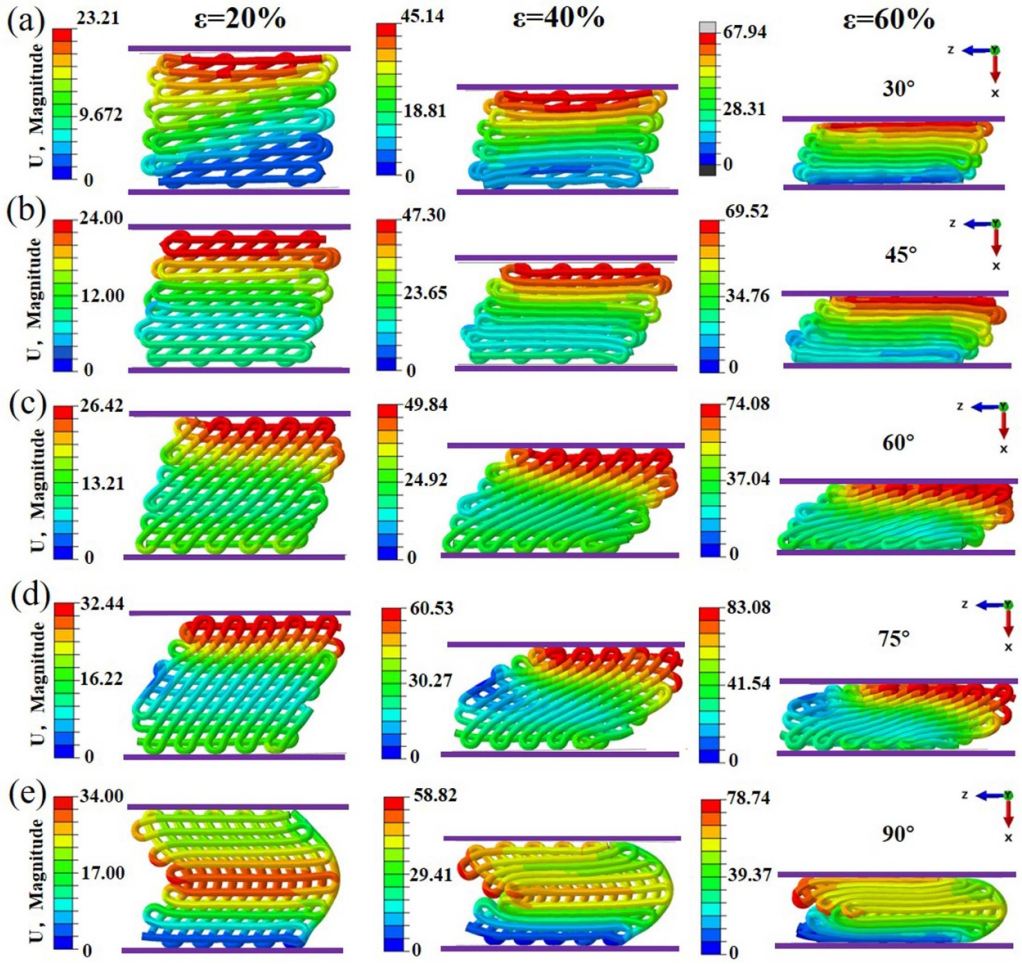

Figure 5. The simulation diagram of the compression test of silicone rubber modular structures printed at different rotation angles under strain (ε) of 20%, 40%, and 60%.

of the hole wall, leading to a plateau stage where the stress remains almost constant; the third stage is the densification stage, resulting from the rapid change in modulus caused by the compression and densification of filaments. The platform stage absorbs energy without deformation, so it is preferable for the modular sample to have a longer and higher platform stage in order to reduce stress fluctuations. Stress variations are minimized because of the printing structure's consistent and well-organized morphology. As a result, all of the modular samples' stress-strain curves in figure 6(b) have a large plateau region (more than 15%), demonstrating the high mechanical buffering capacity of these samples. Figure 6(c) makes it evident that the elastic modulus exhibits a normal distribution pattern as the printing angle increases gradient-wise and achieves its greatest value at 0–90°. This is due to the sample structure's 90° symmetry and the strongest filament-to-filament bonding, which produces a more uniform distribution of stress. As was previously indicated, other samples with the same structure but the opposite filament direction have similar mechanical properties. The error bars in the first two graphs show the range of errors from several experiments, primarily originating from two factors: 1. Because it is impossible to guarantee that every sample is precisely the same during the printing process, there may be variations in modulus. 2. Incorrect readings in experiments on compression. These PDMS modular samples are examples of macroporous materials, which typically have moderate mechanical strength but good stress relaxation. Since PDMS products are frequently utilized in platform stages, we decided to conduct stress relaxation experiments at a strain of 35%. Figure 6(d) displays the stress relaxation curves for these modular samples. It is evident that as time goes on, the stress progressively drops and eventually settles to a fairly steady amount. Both the diffusion and escape of gas in the pores as well as the relaxing of the PDMS matrix material occur during the compression process. As seen in figure 6(e), the modular samples' stress relaxation rates vary, but none of them go above 30%. The aforementioned findings demonstrate that modular Bouligand decomposition structures with gradient changes in mechanical properties may be effectively produced by 3D printing. These printed modular structures can be freely integrated to create specially designed Bouligand structures that are tailored locally (figure S5).

In addition to controlling filament angles during printing, the mechanical properties of these modular samples can also be regulated by adjusting other printing parameters. Taking

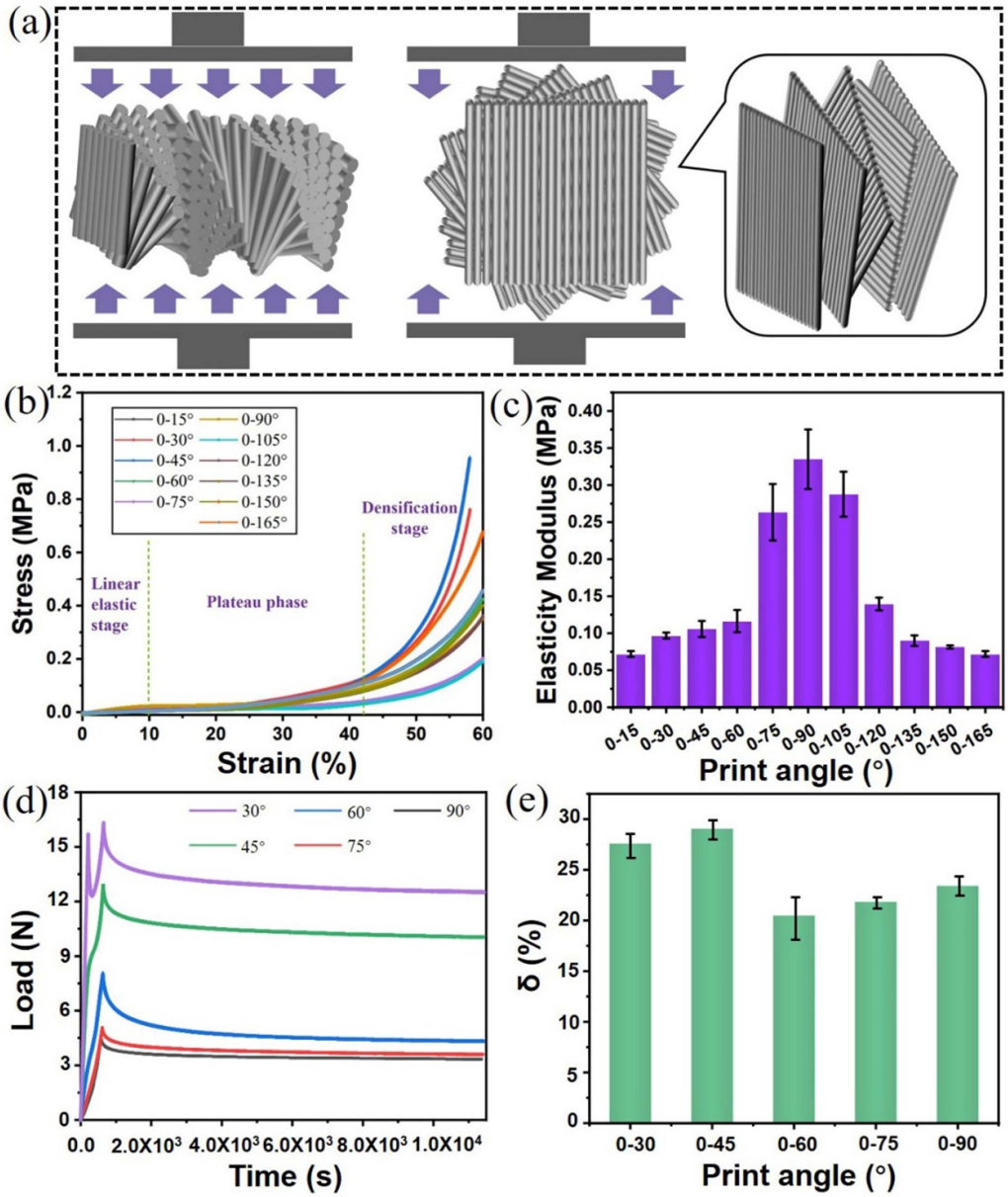

Figure 6. Compressive mechanical properties of printed modular samples with different filament angles. (a) Schematic illurstration of the compression process of the Bouligand structure and its decomposition structures. (b) Compressive stress-strain curves of printed modular samples. (c) Elastic modulus of printed modular samples. (d) Stress relaxation curves of printed modular samples. (e) Corresponding stress relaxation rate.

a 0–90° sample as an example, the compression properties of the printed modular samples with varying filament spacing (ranging from 0.8 mm to 2.4 mm, with 0.4 mm intervals) are analyzed. As depicted in figures 7(a) and (b), the porosity of the modular sample gradually increases and the elastic modulus gradually decreases as the spacing between filaments increases. The elastic modulus of the printed modular sample decreases as the spacing between filaments increases. When the spacing between filaments is 2.4 mm, the modulus of the modular sample is less than 0.2 MPa. When the spacing between filaments is 0.8 mm, the modulus of the modular sample exceeds 0.8 MPa. The compressive stress-strain curves of the printed samples in figure 7(a) reveal that the mechanical strength of the printed modular sample is at its peak when the spacing between filaments is 0.8 mm. However, there is a lack of distinct platform areas, indicating poor mechanical buffering performance of the printed sample at this spacing. For the printed sample with a filament spacing of 2.0 mm, although there is a wider plateau area in the compressive stress-strain curve, the yield stress of this sample is only 0.05 MPa, which is also not conducive to practical applications. For the printed sample with a filament spacing of 1.2 mm, the compressive stress-strain curve exhibits a broad plateau region and a yield stress of 0.15 MPa. The phenomenon described above occurs because the lateral constraint force between adjacent filaments increases as the distance between them decreases.

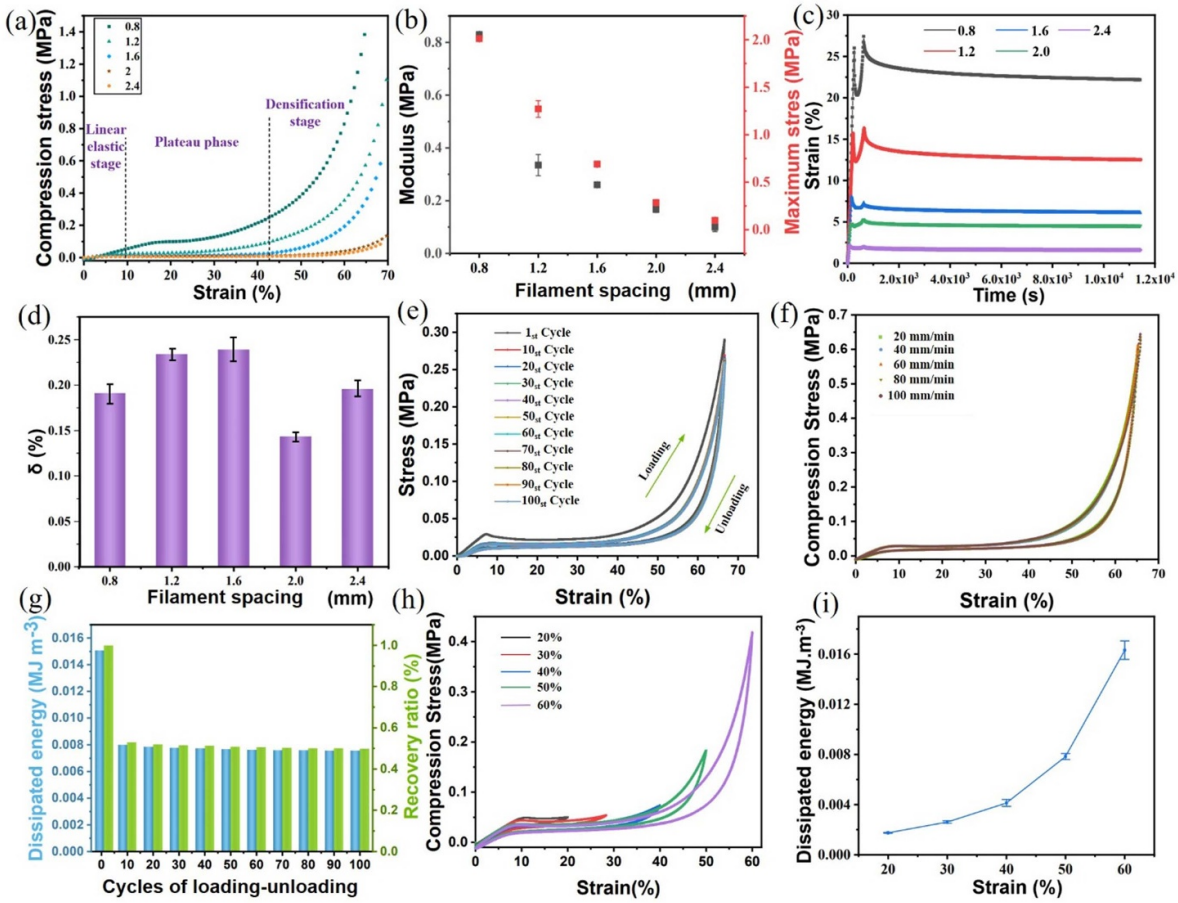

Figure 7. Effect of filament spacing on the mechanical properties of printed modular samples. (a) Stress-strain curves of 0–90° samples with different filament spacing. (b) Elastic modulus and maximum stress of 0–90° samples with different filament spacing. (c) Stress relaxation curves of 0–90° samples with different filament spacing under the strain of 35%. (d) Corresponding stress relaxation rate. (e) 100 times cyclic compression curve of 0–90° printed modular sample. (f) The cyclic compression curve of the 0–90° printed sample under different compression speeds. (g) Dissipated energy and recovery ratio of 0–90° printed modular sample. (h) Cyclic compression curves of 0–90° printed structures under different strains. (i) Corresponding dissipated energy.

This makes it less likely for the sample to yield, resulting in a less pronounced buckling effect. When the filament spacing is approximately 1.2 mm, the printed modular sample generally exhibits a broader plateau area in the compressive stress-strain curve and higher yield strength. This makes it more suitable for the production of cushioning and damping materials. The spacing between printed filaments significantly affects the mechanical properties of the printed sample. This parameter can be adjusted within a certain range to meet various practical application needs.

Similarly, a stress relaxation experiment was conducted on the printed samples using a 35% strain. The stress relaxation curves of the printed samples with varying filament spacing are depicted in figure 7(c). It can be observed that as time passes, the stress of the printed samples gradually decreases and then stabilizes at a relatively constant value. The stress value gradually decreases as the filament spacing increases, which is attributed to the reduction in the number of filaments and nodes. The stress relaxation rates of the printed samples are depicted in figure 7(d). The 0–90° structure sample exhibits a minimum stress relaxation rate of approximately 13% with varying filament spacing, while the maximum rate does not exceed 25%. The compression cycle test results are shown in figure 7(e). Taking the 0–90° printing structure as an example, the compression frequency is 100 cycles. As PDMS is a viscoelastic material, a significant hysteresis loop is observed in the cyclic stress-strain curve. This is because the deformation movement must overcome significant resistance, and external forces are transformed into heat energy, leading to energy dissipation. The speed of compression does not significantly impact the compression process, as shown in figure 7(f). This is because when the loading rate is low and uniformly distributed, the compression behavior of the printed sample is stable, and the change in strain rate may have a minimal impact on the compression behavior. As shown in figure 7(g), after 100 compression cycles, the dissipation energy and recovery rate remain relatively stable. Except for the noticeable stress relaxation phenomenon in the printed sample after the first 10 cycles of compression, the difference in subsequent compression processes is less than 3%. Figures 7(h) and (i) display the cyclic compression curves of the 0–90° printed modular sample under different strains. Although the dissipated

energy steadily increases with increasing strain, the highest values do not exceed 0.4 MPa. From this, a series of modular printed samples with varying mechanical properties were obtained by adjusting the interlayer filament routing angle and filament spacing. The range of gradient mechanical performance changes can meet the application requirements for buffering and energy-absorbing structures. It can be assembled into arrays with different mechanical performance gradients according to specific requirements (see figure S6).

5. Conclusions

This work used DIW printing technology to develop and create a number of modular Bouligand decomposition structures. To achieve modular samples with consistent morphology, a traditional PDMS ink system appropriate for DIW printing method was utilized. Excellent shear thinning behavior of the ink system was shown by rheological performance tests. Furthermore, the ink satisfies the DIW 3D printing requirements effectively since its storage modulus under mild shear stress is greater than its loss modulus. After much consideration, the following were found to be the ideal printing settings for this ink system: a 410 μm inner diameter printing nozzle, 350 μm layer thickness, 1.2 mm filament spacing, extrusion pressure of 0.15 MPa, and printing speed of 5.0 mm s^{-1}. An effective way to control the mechanical properties of a sequence of modular Bouligand structures is to vary the angle at which the filaments of consecutive layers lie. The results of the compression tests show that the printed modular constructions have a greater elastic modulus when the filament angle is near to 0–90°. The sample's mechanical characteristics can be preserved under cyclic compression. The elastic modulus of printed PDMS samples drops with increasing filament separation, and the stress at the same strain likewise decreases. The 3D-printed PDMS modular Bouligand structures can be assembled into gradient-buffered energy-absorbing structures similar to the Bouligand structure. This allows for the regulation of local mechanical properties to meet complex energy-absorbing needs. Although we have completed the necessary experimental design and performance verification using PDMS, the core innovative ideas of this work can also be applied to other AM materials and technologies, including laser AM, metal materials, and ceramic materials.

6. Future perspectives

3D printing is a rapid prototyping technique that uses 3D drawing software to create and print 3D structures layer by layer. Compared to traditional manufacturing methods, 3D printing offers advantages such as diversity, high accuracy, reduced time consumption, and conservation of raw materials. The advancement of 3D printing has made it possible to create complex structural materials and metamaterials. This has had a positive impact on research fields such as electromagnetism, structural engineering, biology, acoustics, and thermodynamics. In addition to mechanical properties, structural materials often have other physical and chemical performance requirements for various application environments and processing conditions. With the continuous development of aerospace, transportation, energy, and power fields, traditional structural materials are constantly evolving to meet the demands of new advancements. High-performance structural materials are an essential foundation for the application of industrial manufacturing. By integrating the most recent 3D metamaterial microarchitecture design concepts and leveraging advanced 3D printing technology, it is feasible to tailor the mechanical properties of materials. These new concept materials will exhibit unique characteristics, such as being ultra-light, ultra-stiff, having a negative Poisson's ratio, a negative compressibility, and stimulus responsiveness.

Acknowledgments

The authors are grateful for the financial support from the National Key Research and Development Program of China (2022YFB4600102), the strategic priority research program of the Chinese Academy of Sciences(XDB0470000), Western Young Scholars Foundations of the Chinese Academy of Sciences, the National Natural Science Foundation of China (52175201, 52108410), Project ZR2023ME061 supported by Shandong Provincial Natural Science Foundation.

Author's contribution

Junfeng Xiao: Experiment, Data curation. Mengxing Zhang: Experiment, Data curation. Fei Zhai: Ideas, Data curation, Writing-Original Draft, Experiment. Hongrui Wei: FEA analysis. Sen Liu: Experiment. Peng Wang: Writing-Review & Editing, FEA analysis. Zhiyang Liu: FEA analysis. Zhongying Ji: Writing-Review & Editing, Data curation. Xiaolong Wang: Writing-Review & Editing, Project administration, Supervision.

Conflict of interest

The authors declare that they have no known competing financial interests or personal relationships that could have appeared to influence the work reported in this paper.

ORCID iD

Fei Zhai https://orcid.org/0000-0003-3718-7596

References

[1] Tanaka K and Chujo Y 2013 Chemicals-inspired biomaterials: developing biomaterials inspired by material science based on POSS *Bull. Chem. Soc. Japan* **86** 1231–9

[2] Tony A, Badea I, Yang C, Liu Y, Wells G, Wang K, Yin R, Zhang H and Zhang W 2023 The additive manufacturing approach to polydimethylsiloxane (PDMS) microfluidic devices: review and future directions *Polymers* **15** 1926

[3] Eduok U, Faye O and Szpunar J 2017 Recent developments and applications of protective silicone coatings: a review of PDMS functional materials *Prog. Org. Coat.* **111** 124–63

[4] Liu C and Ding J 2021 Material extrusion 3D printing of carbon material reinforced PDMS matrix composites and their mechanical properties *49th SME North American Manufacturing Research Conf.* vol 53 pp 450–5

[5] Mazurek P, Vudayagiri S and Skov A L 2019 How to tailor flexible silicone elastomers with mechanical integrity: a tutorial review *Chem. Soc. Rev.* **48** 1448–64

[6] Hinton T J, Hudson A, Pusch K, Lee A and Feinberg A W 2016 3D printing PDMS elastomer in a hydrophilic support bath via freeform reversible embedding *ACS Biomater. Sci. Eng.* **2** 1781–6

[7] McCoul D, Rosset S, Schlatter S and Shea H 2017 Inkjet 3D printing of UV and thermal cure silicone elastomers for dielectric elastomer actuators *Smart Mater. Struct.* **26** 125022

[8] Zhao T, Yu R, Lo S, Li X, Zhang Y, Yang X, Zhao X, Wang C, Liu Z and Dou R 2019 Superstretchable and processable silicone elastomers by digital light processing 3D printing *ACS Appl. Mater. Interfaces* **11** 14391–8

[9] Dahlberg T, Stangner T, Zhang H, Wiklund K, Lundberg P, Edman L and Andersson M 2018 3D printed water-soluble scaffolds for rapid production of PDMS micro-fluidic flow chambers *Sci. Rep.* **8** 3372

[10] Thrasher C J, Schwartz J J and Boydston A J 2017 Modular elastomer photoresins for digital light processing additive manufacturing *ACS Appl. Mater. Interfaces* **9** 39708–16

[11] Zhai F, Feng Y, Li Z, Xie Y, Ge J, Wang H, Qiu W and Feng W 2021 4D printed untethered self-propelling soft robot with tactile perception: rolling, racing, and exploring *Matter* **4** 3313–26

[12] Song L, Lu A, Feng P and Lu Z 2014 Preparation of silicone rubber foam using supercritical carbon dioxide *Mater. Lett.* **121** 126–8

[13] Roh S, Parekh D P, Bharti B, Stoyanov S D and Velev O D 2017 3D printing by multiphase silicone/water capillary inks *Adv. Mater.* **29** 1701554

[14] Xu X, Fang Z, Jin B, Mu H, Shi Y, Xu Y, Chen G, Zhao Q, Zheng N and Xie T 2023 Regenerative living 4D printing via reversible growth of polymer networks *Adv. Mater.* **35** 2209824

[15] Wu H, Chen P, Yan C, Cai C and Shi Y 2019 Four-dimensional printing of a novel acrylate-based shape memory polymer using digital light processing *Mater. Des.* **171** 107704

[16] Bhattacharjee N, Parra-Cabrera C, Kim Y T, Kuo A P and Folch A 2018 Desktop-stereolithography 3D-printing of a poly (dimethylsiloxane)-based material with Sylgard-184 properties *Adv. Mater.* **30** 1800001

[17] Femmer T, Kuehne A J and Wessling M 2014 Print your own membrane: direct rapid prototyping of polydimethylsiloxane *Lab Chip* **14** 2610–3

[18] Zhou L, Gao Q, Fu J, Chen Q, Zhu J, Sun Y and He Y 2019 Multimaterial 3D printing of highly stretchable silicone elastomers *ACS Appl. Mater. Interfaces* **11** 23573–83

[19] O'Bryan C S, Bhattacharjee T, Hart S, Kabb C P, Schulze K D, Chilakala I, Sumerlin B S, Sawyer W G and Angelini T E 2017 Self-assembled micro-organogels for 3D printing silicone structures *Sci. Adv.* **3** e1602800

[20] Muthusamy M, Safaee S and Chen R 2018 Additive manufacturing of overhang structures using moisture-cured silicone with support material *J. Manuf. Mater. Process.* **2** 24

[21] Porter D A, Cohen A L, Krueger P S and Son D Y 2018 Additive manufacturing with ultraviolet curable silicones containing carbon black *3D Print. Addit. Manuf.* **5** 73–86

[22] Zhai F, Feng Y, Zhou K, Wang L, Zheng Z and Feng W 2019 Graphene-based chiral liquid crystal materials for optical applications *J. Mater. Chem.* C **7** 2146–71

[23] Lewis J A 2006 Direct ink writing of 3D functional materials *Adv. Funct. Mater.* **16** 2193–204

[24] Zhu X *et al* 2023 Stress relaxation behavior of 3D printed silicone rubber foams with different topologies under uniaxial compressive load *Compos. Commun.* **38** 101475

[25] Van Meerbeek I M, Lenhardt J M, Small W, Bryson T M, Duoss E B and Weisgraber T H 2022 Compressive properties of silicone Bouligand structures *MRS Bull.* **48** 325–31

[26] Wu A S, Small W, Bryson T M, Cheng E, Metz T R, Schulze S E, Duoss E B and Wilson T S 2017 3D printed silicones with shape memory *Sci. Rep.* **7** 4664

[27] Wen S, Chen S, Gao W, Zheng Z, Bao J, Cui C, Liu S, Gao H and Yu S 2023 Biomimetic gradient Bouligand structure enhances impact resistance of ceramic-polymer composites *Adv. Mater.* **35** 2211175

[28] Yang Y, Chen Z, Song X, Zhang Z, Zhang J, Shung K K, Zhou Q and Chen Y 2017 Biomimetic anisotropic reinforcement architectures by electrically assisted nanocomposite 3D printing *Adv. Mater.* **29** 1605750

[29] Liu S, Dong X, Wang Y, Xiong J, Guo R, Xiao J, Sun C, Zhai F and Wang X 2023 4D printing of shape memory epoxy for adaptive dynamic components *Adv. Mater. Technol.* **8** 2202004

[30] Ji Z, Jiang D, Zhang X, Guo Y and Wang X 2020 Facile photo and thermal two-stage curing for high-performance 3D printing of Poly (Dimethylsiloxane) *Macromol. Rapid Commun.* **10** 2000064

[31] Yang X, Wu T, Liu D, Wu J, Wang Y, Lu Y, Ji Z, Jia X, Jiang P and Wang X 2023 3D printing of release-agent retaining molds *Addit. Manuf.* **71** 103580

[32] Wang H *et al* 2023 A smart mechanical-energy harvesting and self-heating textile device for photo-thermal energy utilization *Ecomat* **5** e12337

[33] Wang J, Sun S, Li X, Fei G, Wang Z and Xia H 2023 Selective laser sintering of polydimethylsiloxane composite *3D Print. Addit. Manuf.* **10** 684–96

[34] Zhang P, Deng B, Zhu K, Zhou Q, Zhang S, Sun W, Zheng Z and Liu W 2022 Wide-temperature range thermoregulating e-skin design through a hybrid structure of flexible thermoelectric devices and phase change materials heat sink *Ecomat* **4** e12253

[35] Truby R L and Lewis J A 2016 Printing soft matter in three dimensions *Nature* **540** 371–8